American Mineralogist, Volume 97, pages 1339–1347, 2012

Raman spectroscopy of $(Ca,Mg)MgSi_2O_6$ clinopyroxenes

Mario Tribaudino,[1,*] Luciana Mantovani,[1] Danilo Bersani,[2] and Pier Paolo Lottici[2]

[1]Dipartimento di Scienze della Terra, Università di Parma, Via Usberti 157/A, 43124 Parma, Italy
[2]Dipartimento di Fisica, Università di Parma, Via Usberti 7/A, 43124 Parma, Italy

Abstract

The Raman spectra of eight clinopyroxenes synthesized along the join diopside-clinoenstatite (Di-Cen, $CaMgSi_2O_6$-$Mg_2Si_2O_6$) were measured. The splitting of the 670 cm^{-1} mode of the A_g symmetry, observed in the composition $Di_{52}En_{48}$ to clinoenstatite, was interpreted as evidence of a $C2/c$-$P2_1/c$ phase transition. The transition was also revealed by deviation from the linear dependence of the peak position vs. composition and by the appearance of several new peaks in the samples richer in clinoenstatite.

Analysis of peak positions vs. structural changes suggests that for the M2 polyhedron, in which Ca substitution for Mg occurs, a different deformation mechanism acts in Ca richer and poorer $P2_1/c$ pyroxenes, and that Ca richer $P2_1/c$ pyroxenes deform with the same mechanism as $C2/c$ pyroxenes. The frequency of the peak at 670 cm^{-1} was found to change linearly with the kinking angle of the tetrahedral chains for $C2/c$ and of the B chain for $P2_1/c$, whereas the position of the peak ascribed to the A chain was little affected by the kinking angle.

Peak broadening in $C2/c$ Ca-rich homogeneous pyroxenes was interpreted to be a consequence of the positional disorder of the Ca and Mg in the M2 cavity: peak broadening increases with increasing Mg content for peaks assigned to M2-O vibrations, but it changes little for peaks assigned to chain bending, which suggests that cation substitution in the M2 cavity occurs with little interaction with the silicate chain. Furthermore peak broadening was observed in intermediate pyroxenes as a consequence of mottled textures, antiphase domains, and compositional inhomogeneity.

Keywords: Pyroxene, Raman spectroscopy, peak position and structure, diopside-clinoenstatite, peak broadening, microstructures

Introduction

Among rock-forming minerals, pyroxenes are of special interest in Earth and Planetary Sciences. They are major constituents in the lower crust and upper mantle, as well as in several chondrites and achondrites. The pyroxene structure, composition, and microtextures can give a wealth of information about the rock in which they are found. Such information can be gathered by careful laboratory investigation through microprobe analysis, electron microscopy, and X-ray diffraction. Often laboratory ex-situ analyses are not possible, however, and other techniques suitable for on-site analysis, such as Raman spectroscopy, are required (Wang et al. 2004). There have been several Raman spectroscopic studies performed on pyroxenes (Mernagh and Hoatson 1997; Huang et al. 2000; Wang et al. 2001; Stalder et al. 2009; Tribaudino et al. 2011). The experimental findings were compared to a well-characterized reference material to obtain the composition of pyroxenes, from the quadrilateral pyroxene systems, $Mg_2Si_2O_6$–$Fe_2Si_2O_6$–$CaMgSi_2O_6$–$CaFeSi_2O_6$. The peak positions in these studies were found to be linearly related to composition; however, a linear correlation is not expected in the presence of a phase transition. Instead, a step at the transition or a change in slope in the different phase fields should be expected. A phase transition induces an excess of free energy, which results in compositional changes in a nonlinear manner and affects the frequencies of the modes (e.g., Iezzi et al. 2010). Moreover, further modes appear because of the decrease in symmetry.

A $C2/c$ to $P2_1/c$ phase transition in pyroxenes occurs between augite and pigeonite because of the substitution of Ca by Fe and/or Mg. Studies on the compositionally induced C to P phase transition in quadrilateral pyroxenes are difficult due to the presence of a wide miscibility gap between Ca-rich and Ca-poor clinopyroxenes: natural intermediate samples, namely, subcalcic augite, are invariably affected by some kind of exsolution textures. Exsolution gives broader and less resolved Raman peaks but can provide potential information on the microstructure of pyroxenes.

In this work, a Raman spectroscopic study was performed on a set of synthetic samples that were synthesized in hypersolvus along the iron-free join diopside-clinoenstatite (Di-Cen, $CaMgSi_2O_6$-$Mg_2Si_2O_6$) and were well characterized previously by transmission electron microscopy (TEM) and X-ray diffraction (XRD) (Tribaudino 2000; Tribaudino et al. 2002, 2005). The diopside-clinoenstatite pyroxenes have the $C2/c$ diopside structure to about $Di_{60}En_{40}$ (Tribaudino 2000) and a $P2_1/c$ structure for higher clinoenstatite content. A large miscibility gap is present in the system, enabling solid solution only close to the solidus (Newton et al. 1979). The aim of this work is to relate Raman peak positions to chemical composition and crystal structure, to define and model spectral changes due to the phase

* E-mail: mario.tribaudino@unipr.it

transition, and to relate peak broadening to microstructure and compositional disorder.

EXPERIMENTAL METHODS

Sample characterization

The clinopyroxenes investigated herein were synthesized in a furnace at 1 atm of pressure and in a piston cylinder at higher pressures. Characterization was done previously using SEM-EDS microprobe analysis (on polished samples), TEM and powder and single-crystal XRD (see Table 1 references).

TEM examination of clinopyroxenes along the join showed that they are quite homogeneous from diopside to $Di_{70}En_{30}$; however, mottled textures appeared for samples with a higher Mg content (up to $Di_{40}En_{60}$), which was preliminary interpreted as evidence of unmixing probably due to spinodal decomposition. The intermediate pyroxenes along the join diopside-clinoenstatite were synthesized in a narrow hypersolvus field; they entered the solvus during cooling at $T \sim 1400$ °C. At such temperatures, even under extremely fast cooling conditions, mottled textures presumably due to spinodal decomposition were formed. TEM selected area diffraction patterns with reflections violating the *C* extinction rules (*h*+*k* odd) were present in thin flakes with an average Mg content higher than that of $Di_{60}En_{40}$. Areas of *P* symmetry appeared at this composition. For compositions between $Di_{60}En_{40}$ and $Di_{50}En_{50}$, a coexistence of *P* antiphase domains a few nanometers in size with large boundaries of *C* structure were found. Antiphase domains were still present in samples with a higher Mg content, but the size of these domains was up to several micrometers in $Di_{15}En_{85}$. These domains form during cooling from a high-temperature $C2/c$ structure to a room-temperature $P2_1/c$ structure and are interpreted as evidence of a phase transition at room temperature (Carpenter 1978; Tribaudino 2000). A locally increased Ca concentration and a $C2/c$ structure were observed at the boundaries of these domains (Carpenter 1978; Moore et al. 2001). The reported TEM microstructures in intermediate compositions induce significant disorder due to strain related to compositional modulations. Twinning at the micro- or nanoscale was also found (Tribaudino 2000).

$Di_{59}En_{41}$ *h*+*k* odd reflections were not found in the X-ray diffraction analysis; they appeared only as weak peaks in $Di_{52}En_{48}$ and became stronger in $Di_{40}En_{60}$ (Tribaudino et al. 2003).

Raman spectroscopy

Raman spectroscopy was performed on polished samples using a Jobin-Yvon Horiba LabRam microRaman with an 1800 line/mm grating and a Synapse detector with a 1024 pixel width. The 632.8 nm line of a He-Ne laser was used for excitation. A filter wheel was used to reduce the laser power on the sample from 20 to 1 mW or less. The frequency calibration was performed against the Raman peak of silicon. A 100x objective with a 0.9 numerical aperture and a confocal hole 200 µm in size was used. Spatial resolution was ~1 µm, and the spectral resolution was 2 cm^{-1}. The decay of the Raman signal in the above setup was estimated to be nearly 5 µm in depth resolution. Due to the small grain size no attempt was made to measure oriented crystals. The peak positions were obtained from baseline-corrected spectra by a least-squares spectral peak curve fitting routine using the computer program Labspec. A Lorentzian profile was used in the peak profile analysis. A minimum of 5 spectra were collected for each sample at different positions, showing for each composition differences in peak position below 1 cm^{-1}.

Peak profiles are reported in Figure 1; peak positions and linewidths calculated from the average of the measured spectra are given in Table 2.

TABLE 1. Previous investigations (TEM, room-temperature, high-pressure and high-temperature single-crystal and powder X-ray diffraction) and microstructural characterization of the samples studied in this work

Composition	TEM microstructure	Source synthesis	XRD	TEM
Di_{100}	homogeneous	1	1	
$Di_{80}En_{20}$	homogeneous	2	1, 3, 4	1
$Di_{70}En_{30}$	homogeneous	5	5	6
$Di_{66}En_{34}$	local mottled textures	2	2	6
$Di_{59}En_{41}$	mottled textures, nanometer-sized antiphase domains together with flakes without antiphase domains	6	5	5
$Di_{52}En_{48}$*	mottled textures, nanometer-sized antiphase domains	4	4, 5	4
$Di_{40}En_{60}$	mottled textures, micrometer-sized antiphase domains	4	4, 5	4
$Di_{15}En_{85}$	homogeneous, several micrometer-sized antiphase domains	7	7, 8	7

Note: Data from: (1) Tribaudino et al. (2000); (2) Tribaudino et al. (1989); (3) Benna et al. (1990), (4) Tribaudino et al. (2003); (5) Tribaudino et al. (2005); (6) Tribaudino (2000); (7) Tribaudino and Nestola (2002); and (8) Tribaudino et al. (2002).
* Contains 0.04 atoms Al apfu.

RESULTS

Raman spectra for pyroxenes with a changing Mg content from diopside to clinoenstatite are shown in Figure 1. From factor-group analysis, $C2/c$ and $P2_1/c$ pyroxenes are expected to exhibit 30 and 60 active Raman peaks, respectively (Wang et al. 2001); however, most of these peaks are too weak to be observed experimentally. Even though as many as 21 peaks could be identified, only five of them (at 230, 330, 400, 670, and 1010 cm^{-1}) were followed throughout the join. The number of peaks is comparable to the number studied in a set of natural and synthetic quadrilateral pyroxenes by Huang et al. (2000). Table 2 reports the position and the symmetry attribution of the Raman peaks for all the samples.

The pyroxene spectrum is generally divided into three re-

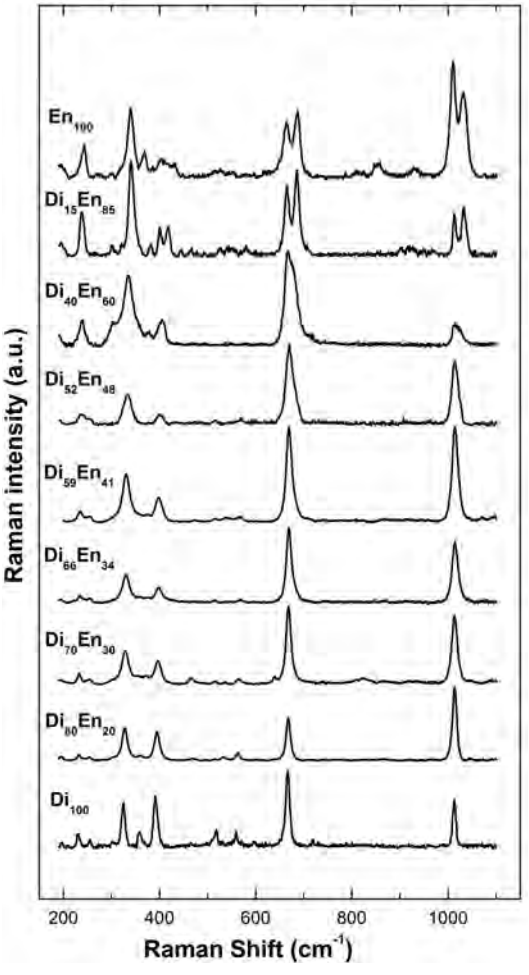

FIGURE 1. Raman spectra of the clinopyroxenes studied here. Reference spectrum of clinoenstatite from Downs (2006) Raman data repository.

TABLE 2. Position of the Raman peaks

	Di_{100}	$Di_{80}En_{20}$	$Di_{70}En_{30}$	$Di_{66}En_{34}$	$Di_{59}En_{41}$	$Di_{52}En_{48}$	$Di_{40}En_{60}$	$Di_{15}En_{85}$	Cen	
ν_1	138									A_g
ν_2	160					162				B_g
ν_3	181	183	182		182	182	182		179	A_g
ν_4	197	195	194	193	192	19	189	196	195	B_g
ν_5	231	233	233	235	235	238	238	239	244	A_g, B_g
ν_6	255	254	253	254	255	255				A_g
ν_7	302						303	301	301	A_g, B_g
ν_8	324	328	329	330	331	334	335	341	342	A_g
ν_9	359	360							369	B_g
ν_{10}								382	385	B_g Cen
ν_{11}	392	395	396	398	398	401	405	401	403	A_g
ν_{12}								418	417	B_g Cen
ν_{13}								445	431	A_g Cen
ν_{14}		469	466							B_g
ν_{15}	516									B_g
ν_{16}		534								A_g
ν_{17}	559	563	566		567				554	B_g
ν_{18}	666	668	668	669	669	671*	666	665	665	A_g
ν_{19}							676	685	688	A_g
ν_{20}	1013	1014	1013	1014	1014	1014.5	1013	1014	1013	A_g
ν_{21}								1033	1033	A_g, B_g

Notes: The standard deviations of the average of the peak positions were lower than the spectral resolution (2 cm^{-1}). Clinoenstatite Raman data here and in Table 4 from Ulmer and Stalder (1999). Peak assignment was done on the basis of quantum-mechanical simulations by Prencipe et al. (2012) and Yu et al. (2010), for *C*2/*c* and $P2_1/c$ pyroxenes, respectively. Cen found in Yu et al. (2010) simulations and not in Prencipe et al. (2012).
* Unsplit peak fitting.

gions: (1) T-O stretching peaks near 1000 cm^{-1}, including an intense peak at 1010 cm^{-1} ascribed to stretching modes of Si and nonbridging O1 and O2 atoms (Fig. 2) within the SiO_4 tetrahedron (R1 region according to Wang et al. 2001); (2) peaks due to chain bending and/or stretching at 500–700 cm^{-1} [R2 and R4 in Wang et al. (2001)], including the most intense peak at 665 cm^{-1} in diopside and a few weak peaks around 500 cm^{-1}; and (3) peaks below 500 cm^{-1} generally ascribed to non-tetrahedral cation vs. oxygen stretching of M1-O and M2-O bonds (Huang et al. 2000). Modes at 400 and 330 cm^{-1} are also included in this region [R3 and R5 regions in Wang et al. (2001)]. Quantum-mechanical simulation shows that such bending and stretching modes are highly correlated with chain motion, and in some cases, such as the peak at 135 cm^{-1}, the chain bending occurs with M1 and M2 cations at rest (Prencipe et al. 2012).

The Raman spectrum for synthetic diopside (Di_{100} in Fig. 1) was found to be very similar to that obtained for natural and synthetic diopside as reported in previous papers (Etchepare 1970; Swamy et al. 1996; Huang et al. 2000; Chopelas and Serghiou 2002; Prencipe et al. 2012).

The spectra of diopside and $Di_{59}En_{41}$ are similar despite the substitution of Ca with Mg. At a lower Ca content, some peaks became asymmetric. In the $Di_{40}En_{60}$ spectrum, the peak splitting for the intense peak at 670 cm^{-1} is evident.

As suggested by Wang et al. (2001) for quadrilateral pyroxenes, the splitting of the 670 cm^{-1} mode is related to structural changes involving the silicate chains. The tetrahedral chains in the *C*2/*c* structure are symmetrically equivalent, whereas in the

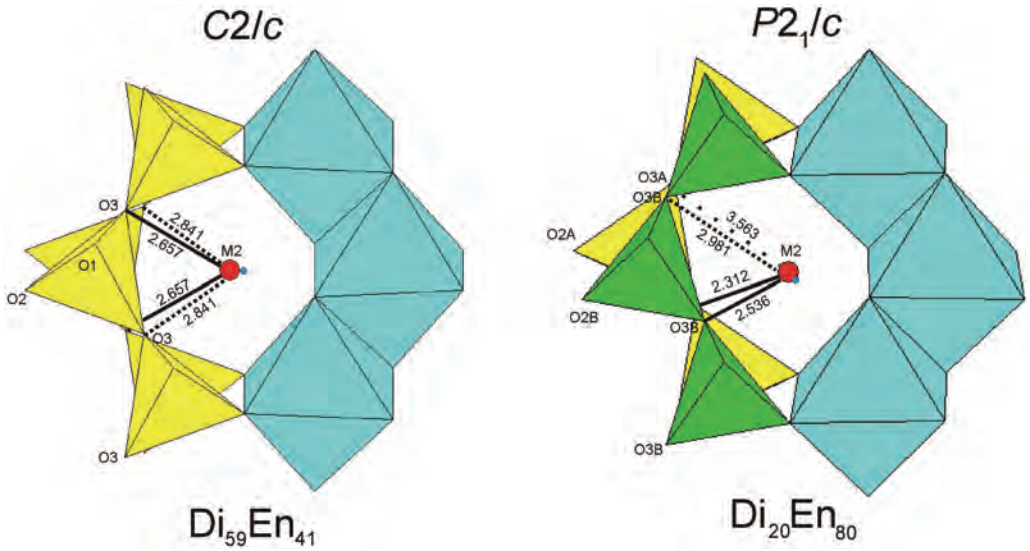

FIGURE 2. M2 polyhedron and M2-O3 distances in *C*2/*c* $Di_{59}En_4$ and $P2_1/c$ $Di_{20}En_{80}$. Cation-oxygen distances are dashed and dotted between weakly bonded atoms. The smaller M2′ site is shown as a dot near the larger M2 site. (Color online.)

$P2_1/c$ structure there are two symmetrically independent chains with different deformation angles and Si-O bond lengths (Fig. 2). Because the 670 cm^{-1} peak is related to the bending motion of the tetrahedral chain, a splitting of the 670 cm^{-1} peak was expected from the presence of two independent tetrahedral chains. Raman bands at lower frequencies, which are related to M2 and M1-O motion, did not show peak spitting because of the presence of uniquely symmetric and independent M2 and M1 sites in both $P2_1/c$ and in $C2/c$. The mode splitting at 670 cm^{-1} is therefore evidence in the Raman data of the phase transition of Ca-rich samples from the $C2/c$ to $P2_1/c$ space group, as previously observed using TEM and powder diffraction analysis (Tribaudino 2000; Tribaudino et al. 2003, 2005).

As a marker of the phase transition, the splitting of the 670 cm^{-1} peak was also observed in the pressure-induced phase transition of clinoenstatite (Ross and Reynard 1999), which switched at the same pressure of the $C2/c$ to $P2_1/c$ phase transition observed by X-ray diffraction (Angel et al. 1992). The same splitting is present only in pyroxenes with a P lattice, such as pigeonites and orthopyroxenes (Mernagh and Hoatson 1997; Huang et al. 2000; Wang et al. 2001; Stalder et al. 2009; Tribaudino et al. 2011). Although evidence of the phase transition is found only in Mg-rich samples, the slight asymmetry in the 670 cm^{-1} peak of $Di_{52}En_{48}$ suggests the presence of an underlying peak splitting (Fig. 3). This result is in agreement with previous TEM and X-ray diffraction data (Tribaudino 2000), showing that a partial transformation to P symmetry occurs from $Di_{60}En_{40}$ to a higher Mg content.

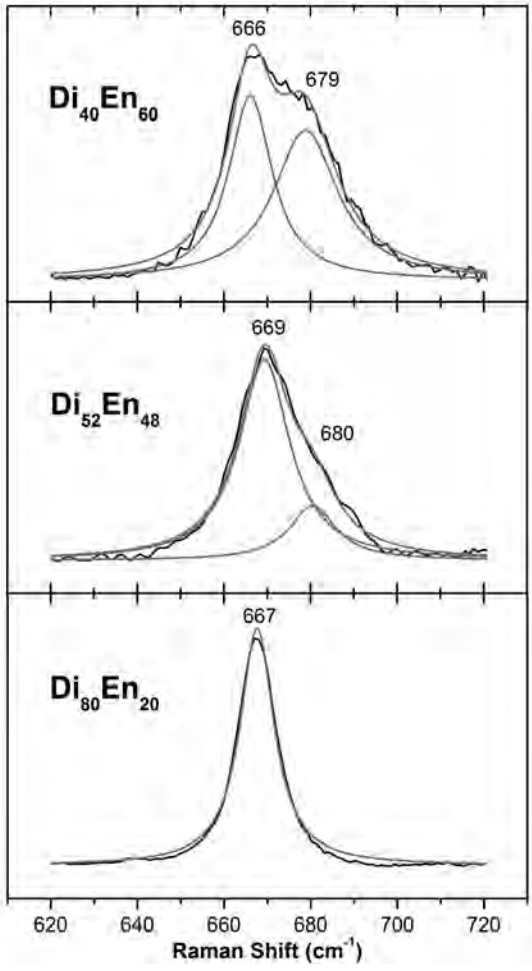

FIGURE 3. Peak deconvolution of the peak at 670 cm^{-1}: (**a**) single unsplit peak at $Di_{59}En_{41}$; (**b**) peak asymmetry at $Di_{52}En_{48}$; and (**c**) peak splitting at $Di_{40}En_{60}$.

Because of the highly defective nature of the $Di_{40}En_{60}$ sample, which had compositional modulations and antiphase domains, its spectrum is rather broad. $Di_{15}En_{85}$, which is the sample richest in Mg that was measured in this work, is homogeneous (Tribaudino et al. 2002) and shows better resolved spectral features; its spectrum is quite similar to that of clinoenstatite (Ulmer and Stalder 2001).

Because of the higher Mg content in clinoenstatite and $Di_{15}En_{85}$, the P structure is revealed both by the greater number of Raman peaks and the change in relative intensities of the peaks at 381, 417, 445, and 1030 cm^{-1}. The changes in the relative intensities with respect to $C2/c$ clinoenstatite are observed with strong intensities only in $Di_{15}En_{85}$ but not in $P2_1/c$ pyroxenes with a higher Ca content, such as $Di_{52}En_{48}$ and $Di_{40}En_{60}$.

In most cases, a structural explanation of the behavior of the vibrational modes through the transition is not straightforward; for example, an apparent peak splitting may simply be due to the onset of a peak characteristic of the $P2_1/c$ symmetry. This apparent peak splitting of the 1010 cm^{-1} mode occurs for presence of a peak at 1030 cm^{-1}, as discussed later.

DISCUSSION

Phase transition

The phase transition can be monitored by following the changes in position of the most intense peaks found in both the $P2_1/c$ and $C2/c$ structures. Peak positions generally show linear changes as a function of composition (Fig. 4). A linear behavior for iron-free quadrilateral clinopyroxenes can be modeled using the following equation

$$\omega = \omega_o + kX_{Di} \quad (1)$$

where k is the wavenumber-composition slope, ω_o is the peak position of the initial composition (clinoenstatite in this case), and X_{Di} is the diopside mole fraction.

In the presence of a phase transition, an excess contribution ($\Delta\omega_{ex}$) is expected because of the changes in the vibrational spectrum of the low-symmetry phase with respect to the high-symmetry phase.

The dependence between frequencies and composition in the low-symmetry region can be described by the following

$$\omega = \omega_o + kX_{Di} + \Delta\omega_{ex} \quad (2)$$

where the excess contribution is expected to change with composition. As a result, compositional changes in the $C2/c$ and $P2_1/c$ phase fields have to be modeled differently.

Table 3 reports the slope and intercept for the modes in the $C2/c$ and $P2_1/c$ pyroxenes. The value of ω for $X_{Di} = 0$ (clinoenstatite end) can be extrapolated using a linear fit of the frequencies measured in the $C2/c$ pyroxenes. This value is significantly

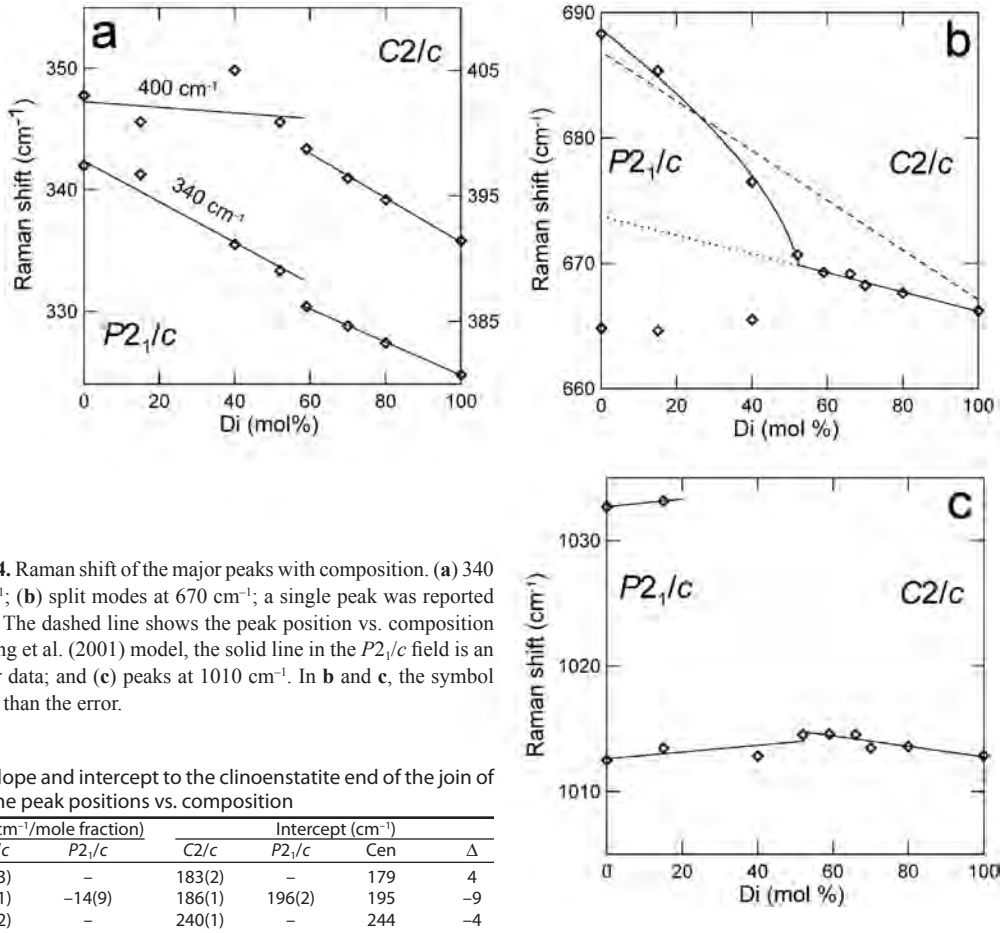

FIGURE 4. Raman shift of the major peaks with composition. (**a**) 340 and 400 cm^{-1}; (**b**) split modes at 670 cm^{-1}; a single peak was reported for $Di_{52}En_{48}$. The dashed line shows the peak position vs. composition from the Wang et al. (2001) model, the solid line in the $P2_1/c$ field is an eye fit to our data; and (**c**) peaks at 1010 cm^{-1}. In **b** and **c**, the symbol size is larger than the error.

TABLE 3. Slope and intercept to the clinoenstatite end of the join of the peak positions vs. composition

	Slope (cm^{-1}/mole fraction)		Intercept (cm^{-1})			
N	*C*2/*c*	$P2_1/c$	*C*2/*c*	$P2_1/c$	Cen	Δ
ν_3	−1(3)	–	183(2)	–	179	4
ν_4	11(1)	−14(9)	186(1)	196(2)	195	−9
ν_5	−9(2)	–	240(1)	–	244	−4
ν_6	4(2)	–	251(1)	–		
ν_8	−15(1)	−17(6)	340(1)	342(1)	342	−2
ν_{11}	−18(2)	5(8)	409(1)	402(2)	403	6
ν_{17}	−20(1)	–	579(1)	–		
ν_{18}	−8(1)	−30(4)	674(1)	689(1)	688	−14
ν_{19}	–	2(1)	–	665(1)	665	
ν_{20}	−4(1)	0(2)	1017(1)	1013(1)	1013	4

Notes: The slope and intercept under the *C*2/*c* columns are calculated with data from diopside up to $Di_{59}En_{41}$; those under the $P2_1/c$ column are calculated from $Di_{40}En_{60}$ to clinoenstatite. The calculation was performed when at least three values were available. Δ is the difference between the value extrapolated from *C*2/*c* to the clinoenstatite end-member and that observed experimentally in clinoenstatite (Ulmer and Stadler 1999).

different from the value observed for clinoenstatite, indicating that the additional contribution from the phase transition is present in the pyroxenes studied here. The additional contribution can also be seen in Figure 4: a step at approximately $Di_{52}En_{48}$ is observed for the 340 cm^{-1} mode, whereas the mode at 400 cm^{-1} shows a change in slope at $Di_{40}En_{60}$; moreover, the split modes at 670 cm^{-1} show both a deviation from the *C*2/*c* trend.

Structural and spectral changes

The relatively large database on crystal structures of synthetic pyroxenes along the join diopside-clinoenstatite enables a correlation to be drawn between the average structure as determined by X-ray diffraction and the Raman spectral modes.

As reported in Table 3, a negative slope was observed for the stronger modes in *C*2/*c*. For $P2_1/c$, a negative slope was observed for the mode at 340 cm^{-1} and in one of the two split modes at 670 cm^{-1}, whereas the frequencies in the other modes are nearly insensitive to compositional changes.

The negative slope for all the strong modes in the *C*2/*c* field (i.e., increasing energy with decreasing Ca content) indicates that an empirical correlation is expected with cell volume and M2-O bond distances. Substitution of Ca with Mg in the M2 polyhedron is the only chemical change in the crystal along the join, resulting in a decrease of 1.5% in cell volume between diopside and $Di_{60}En_{40}$ (Newton et al. 1979). As shown in Figure 5, which reports a collection structural data from literature, the M2-O average bond length decreases from diopside to clinoenstatite both in *C*2/*c* and $P2_1/c$, although there is a change in slope at the transition.

On the other hand, the M1-O average bond lengths do not change, regardless of the symmetry, which is in disagreement with a previous assignment of the M1-O stretching mode at 400 cm^{-1} (Huang et al. 2000). The wavenumber of this mode was found to decrease with Ca content in the *C*2/*c* field and showed a change in Raman shift between the end-members up to 11 cm^{-1}, corresponding to a significant change in energy that should occur after a significant change in M1-O bond lengths. Recent quantum-mechanical simulations in diopside by Prencipe et al. (2012) indicated that this mode cannot be assigned solely to the M1-O motion but is an M1-O vibration interacting with the

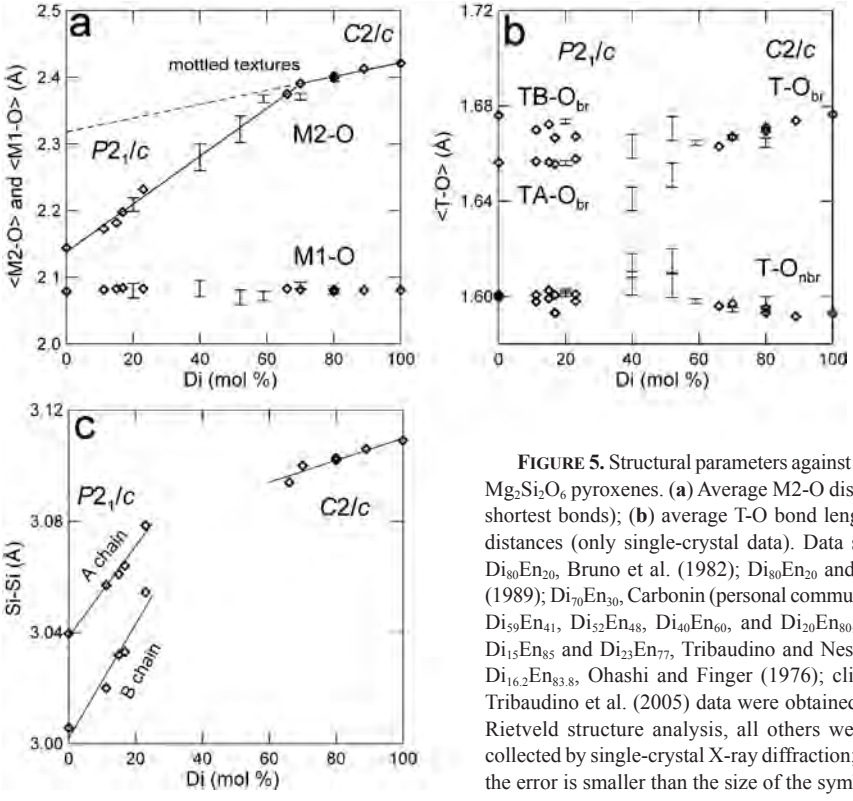

FIGURE 5. Structural parameters against composition in $CaMgSi_2O_6$-$Mg_2Si_2O_6$ pyroxenes. (**a**) Average M2-O distances (average over the six shortest bonds); (**b**) average T-O bond lengths; and (**c**) T-T intrachain distances (only single-crystal data). Data source: Di_{100}, $Di_{89}En_{11}$, and $Di_{80}En_{20}$, Bruno et al. (1982); $Di_{80}En_{20}$ and $Di_{66}En_{34}$, Tribaudino et al. (1989); $Di_{70}En_{30}$, Carbonin (personal communication); $Di_{80}En_{20}$, $Di_{70}En_{30}$, $Di_{59}En_{41}$, $Di_{52}En_{48}$, $Di_{40}En_{60}$, and $Di_{20}En_{80}$, Tribaudino et al. (2005); $Di_{15}En_{85}$ and $Di_{23}En_{77}$, Tribaudino and Nestola (2002); $Di_{11.8}En_{88.2}$ and $Di_{16.2}En_{83.8}$, Ohashi and Finger (1976); clinoenstatite Ohashi (1984). Tribaudino et al. (2005) data were obtained by powder diffraction and Rietveld structure analysis, all others were refined from intensities collected by single-crystal X-ray diffraction; in single-crystal X-ray data the error is smaller than the size of the symbols.

tetrahedral chain. In fact, the assignment of a mode involving M2-O or M1-O motion must also consider the interaction with the tetrahedral chain.

The peak positions after the transition have a different trend with the crystal structure. As shown in Figure 6, the peak frequencies at 340 cm^{-1} are plotted as a function of the M2-O bond length, which was obtained from the single-crystal data. As expected, the negative correlation in the *C*2/*c* symmetry between M2-O bond length and peak position was observed. The negative correlation in the $P2_1/c$ symmetry was found only for compositions rich in Ca, whereas it was not in compositions rich in Mg (Fig. 6). A different trend between $P2_1/c$ Ca-rich ($Di_{52}En_{48}$ and $Di_{40}En_{60}$) and Mg-rich ($Di_{15}En_{85}$ and En_{100}) samples was also found along the Di-Cen join for the β and *c* cell parameters (Tribaudino 2000). In $P2_1/c$ pyroxenes rich in Ca, the *c* parameter does not change, but the β parameter increases steadily from diopside to clinoenstatite, whereas in $P2_1/c$ pyroxenes rich in Mg, *c* decreases while β remains nearly unchanged. Similar to the M2-O vs. peak position of the 340 cm^{-1} mode, the cell parameters show a change at $Di_{40}En_{60}$ instead of at $Di_{60}En_{40}$, where the transition was observed.

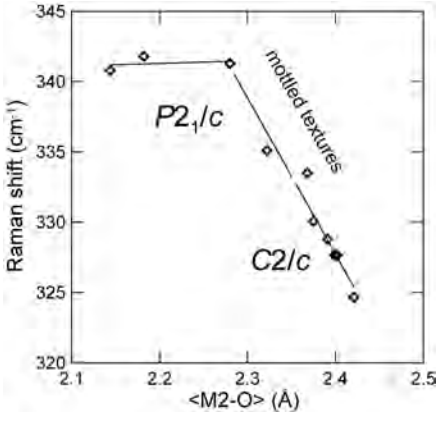

FIGURE 6. Peak position vs. average M2-O distance (over 6 O atoms) of the 340 cm^{-1} mode in $P2_1/c$ and *C*2/*c* pyroxenes.

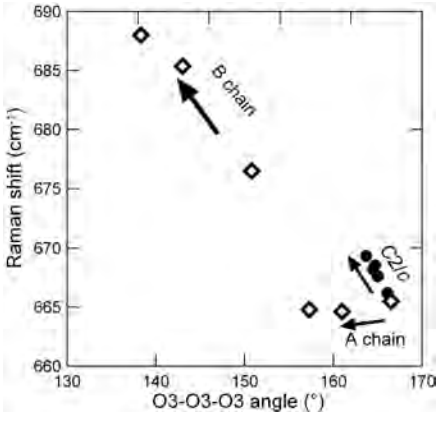

FIGURE 7. Peak position of the mode at 670 cm^{-1} vs. O3-O3-O3 chain kinking angle; full circles: *C*2/*c* structures, open diamonds: $P2_1/c$. The $P2_1/c$ datum at $Di_{52}En_{48}$ was not reported as the Raman peak was refined unsplit.

For the higher energy mode that is related to tetrahedral chain bending at 670 cm^{-1}, a good linear correlation exists in *C*2/*c* between the peak frequency and the O3-O3-O3 kinking angle (Fig. 7); that is, the more the tetrahedral chain is kinked, the higher the energy of the mode. At lower kinking angles, the distance between the T atoms in the tetrahedra decreases slightly (from 3.109 in diopside to 3.094 Å in $Di_{66}En_{34}$) and the repulsion between tetrahedra in the chain increases. The above dependence between the mode at 670 cm^{-1} and the Si-Si distance in pyroxenes was previously observed by Ohashi and Sekita (1982) in a study comparing the Si-O-Si stretching vibration in several synthetic clinopyroxenes.

In the $P2_1/c$ symmetry, however, the kinking angle and the Si-Si distances of both A and B chains decrease with increasing Mg content (Angel et al. 1992). If the trend observed in *C*2/*c* was the same in $P2_1/c$, an increase in energy with increasing clinoenstatite content for both split peaks at 670 cm^{-1} would then be expected; however, the opposite was observed for the lowest energy peak. The higher energy peak can be tentatively ascribed to the bending in the B chain, which has a lower kinking angle and a shorter Si-Si distance. The kinking of the B chain has then a linear correlation with the frequency shift and with the kinking of the *C*2/*c* chain (Fig. 7). On the other hand, the behavior of the lower energy mode cannot be simply related to a structural feature in one of the A and B chains.

The peak at 1010 cm^{-1} was ascribed to a T-O stretching mode with nonbridging atoms. As shown in Figure 5, the T-O non-bridging distances changed little along the join. After the transition, they have almost the same values in the TA and TB tetrahedra, very close to those in the *C*2/*c* T tetrahedron. This result is in agreement with the small change of the mode frequency through the join. On the other hand, as previously discussed by Wang et al. (2001), the mode at 1030 cm^{-1} is not related to chain splitting. The difference in wavenumber between the modes at 1010 and 1030 cm^{-1} cannot be a result of the difference in the tetrahedral bond distance as the relevant changes are negligible.

From the above data, three different trends along the join are found. One trend is that the changes in peak position for *C*2/*c* pyroxenes are linearly correlated with composition and crystal structure. A second trend is that changes for intermediate $P2_1/c$ pyroxenes follow those for *C*2/*c* for the low-energy 340 cm^{-1} mode but show an apparent split in the peak at 670 cm^{-1}. A third trend is that of samples rich in Mg close to the clinoenstatite end-member and a Ca content similar to natural pigeonite. Several new peaks appear for the intermediate $P2_1/c$ pyroxenes, and the 340 cm^{-1} mode has a different dependence on the M2-O average bond length (Fig. 6).

The different trends can be interpreted in the framework of the electron microscope and structural data. The transition from *C*2/*c* to $P2_1/c$ was pinpointed at approximately $Di_{60}En_{40}$ by the appearance of *h*+*k* odd reflections in the electron diffraction and powder diffraction (albeit faint) data. Evidence for a high-pressure and high-temperature transition was also found for

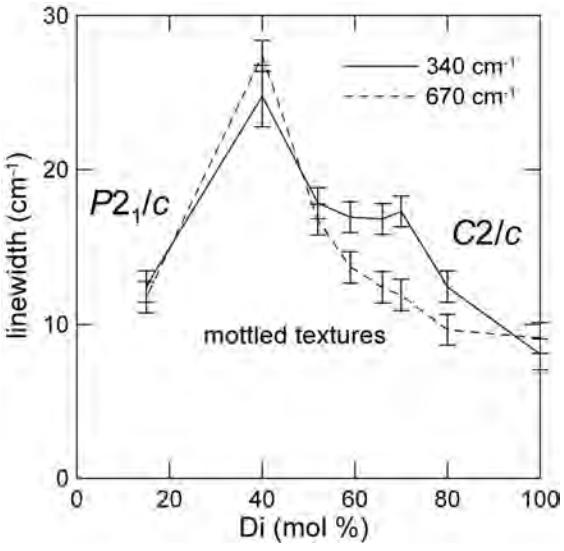

FIGURE 8. Linewidth vs. composition of the peaks at 340 and 670 cm^{-1}.

TABLE 4. Linewidth (FWMH, in cm^{-1}) of the studied peaks

	ν (cm^{-1})	Di_{100}	$Di_{80}En_{20}$	$Di_{70}En_{30}$	$Di_{66}En_{34}$	$Di_{59}En_{41}$	$Di_{52}En_{48}$	$Di_{40}En_{60}$	$Di_{15}En_{85}$
ν_2	161	10(1)					7(1)		
ν_3	182	6(1)	7(1)	7(1)		7(1)	4(1)	6(1)	
ν_4	194		6(1)	19(2)		13(2)	10(1)	13(2)	13(2)
ν_5	236	7(1)	8(1)	8(1)	11(1)	12(1)	17(1)	12(3)	10(2)
ν_6	254	6(1)	9(1)	13(1)	10(2)	10(1)	9(2)		
ν_7	302							14(3)	7(2)
ν_8	333	8(1)	12(1)	16(1)	16(1)	16(1)	17(1)	24(2)	12(1)
ν_9	363	7(1)							
ν_{10}	383								6(1)
ν_{11}	399	9(1)	11(1)	15(1)	15(1)	14(1)	14(1)	15(2)	7(1)
ν_{12}	417								10(1)
ν_{13}	438								5(1)
ν_{14}	467		14(3)	12(2)					
ν_{15}	517	11(1)							
ν_{16}	534		16(3)						
ν_{17}	562	8(1)	12(1)	10(1)		18(5)			
ν_{18}	667	9(1)	10(1)	12(1)	12(1)	14(1)	17(1)	12(1)	11(1)
ν_{19}	683							27(1)	12(1)
ν_{20}	1014	7(1)	9(1)	13(1)	13(1)	13(1)	13(1)	10(1)	8(1)
ν_{21}	1033								13(1)

Notes: Peak width was obtained by averaging the different spectra (minimum of 5) for each composition. The errors represent the standard deviations of the average peak widths. For peaks missing here but present in Table 2, the linewidth could not be estimated, owing to the low intensity of the peaks.

samples with compositions near $Di_{50}En_{50}$ (Fig. 5) (Tribaudino et al. 2001, 2003).

On the other hand, the change of the β and *c* parameters and the spectroscopic behavior suggests that the structural environment at the M2 site changes at approximately $Di_{40}En_{60}$.

The analysis of the intermediate sample structures shows that the size of the M2 polyhedron is decreased by two different mechanisms: (1) in *C*2/*c* pyroxenes, a shift parallel to the **c** axis of the tetrahedral chain, which increases the β angle (Tribaudino et al. 1989, 2005), and (2) in Mg-rich pyroxenes and $P2_1/c$ natural pigeonite (Morimoto and Guven 1970; Angel et al. 1992), a rearrangement of the tetrahedral chains, which release two M2-O bonds (Fig. 2). In pigeonite, the kinking of the A chain is opposite to that of the B chain, with a full release of the furthermost oxygen in the M2 polyhedron so that the M2 site coordination becomes sixfold instead of eightfold, as in Ca-rich pyroxenes. In intermediate $P2_1/c$ pyroxenes, the symmetry is broken, but the decrease in the size of the M2 polyhedron follows the same mechanism as in *C*2/*c* pyroxenes; that is, the shift of the tetrahedral chain results in an increase in the β angle (Tribaudino et al. 2005).

Raman spectroscopy and microstructural features

Peak widths are related to the extent of structural order, and Table 4 and Figure 8 report the peak widths for each composition modes at 340 and 670 cm^{-1}. Sources of disorder in pyroxenes along the join diopside-clinoenstatite are as follows (Tribaudino et al. 2005).

(1) The split M2-M2′ be due to the two different positions of Ca and Mg in the relatively large and distorted M2 polyhedron. In the *C*2/*c* structure, both M2 and M2′ lie along the diad axis with Mg in a local 4+2 coordination, whereas Ca retains its eightfold coordination (Fig. 3) (Rossi et al. 1987; Tribaudino et al. 1989). In the $P2_1/c$ structure, Ca and Mg move off the diad axis, but the local coordination for Ca and Mg is still similar to what is found in *C*2/*c* (Tribaudino and Nestola 2002).

(2) Mottled textures that are a result of incipient spinodal decomposition in $Di_{59}En_{41}$ and $Di_{40}En_{60}$.

(3) Antiphase domains that form in $P2_1/c$ pyroxenes because of the *C*2/*c*-$P2_1/c$ transition during cooling.

Another cause of peak widening is compositional heterogeneity at the sub-micrometric scale. TEM-EDS analysis showed that compositional heterogeneity occurs for compositions between $Di_{59}En_{41}$ and $Di_{40}En_{60}$, whereas the samples outside this compositional range are homogeneous (Tribaudino 2000; Tribaudino et al. 2005). These heterogeneities could be revealed only by the TEM-EDS analysis (Tribaudino 2000), which samples a small area of a few tens of nanometers. On the other hand, SEM-EDS analysis was unable to detect significant compositional heterogeneities in intermediate samples because this analysis can only be determined for sample volumes as small as 1–2 μm^3. The same is true for our Raman data, which has an even larger sampling volume (5–10 μm^3).

M2-M2′ splitting, which increases between diopside and $Di_{60}En_{40}$ (Tribaudino et al. 1989), was responsible for the broadening of the 340 cm^{-1} peak observed within the *C*2/*c* field, which nearly doubled between diopside and $Di_{60}En_{40}$. The linewidth reached a maximum at $Di_{40}En_{60}$ and decreased at higher concentrations of Mg. The increased broadening in the intermediate samples between $Di_{60}En_{40}$ and $Di_{40}En_{60}$ is likely due to the presence of further disorder coming from antiphase domains and mottled textures, together with compositional heterogeneity. On the other hand, the linewidth of $Di_{15}En_{85}$ was very close to that of $Di_{80}En_{20}$; in $Di_{15}En_{85}$ mottled textures were not found and antiphase domains were micrometer sized (Tribaudino et al. 2002).

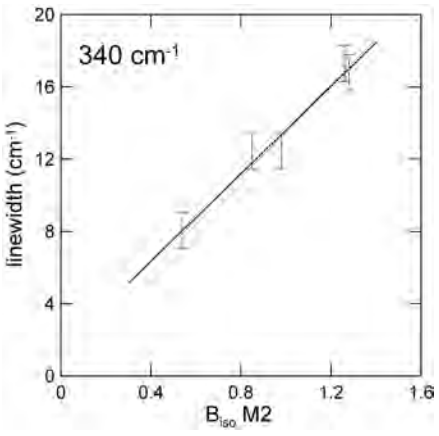

FIGURE 9. Linewidth of the peak for the mode at 340 cm^{-1} vs. B_{iso} (in $Å^2$) of the M2 site atom. Only single-crystal data were used for Di_{100}, $Di_{80}En_{20}$, $Di_{70}En_{30}$, $Di_{66}En_{34}$, and $Di_{15}En_{85}$.

In spite of the highly disordered and heterogeneous nature of the intermediate samples, the peak positions of the Raman spectra collected from the same sample are close enough together that their difference is below spectral resolution. Mottled textures and spinodal decomposition occur with a modulation-length on the order of nanometers, whereas the spatial resolution of our Raman spectroscopy investigation is limited to 5–10 μm^2. Antiphase domains are only crystallographic inhomogeneities with the same composition and crystallography in antiphase; hence, no difference was expected between Raman spectra taken from areas of the crystal in antiphase. However, all microtextures provide some degree of local disorder, which is revealed by broader peaks. The linewidth of the 340 cm^{-1} peak is related to the M2 isotropic site displacement parameter (B_{iso}), as refined by single-crystal diffraction in homogeneous samples. Displacement parameters in the crystallographic structure refinement describe dynamic or static displacement of atoms in crystals (Trueblood et al. 1996). The linear behavior shown in Figure 9 indicates that the linewidth of the peak at 340 cm^{-1} is a probe for static positional disorder of the M2 site. The isotropic displacement parameter depends mostly on the Ca-Mg disorder within the M2 site (Tribaudino et al. 1989; Benna et al. 1990; Tribaudino and Nestola 2002) and increases with Mg content in *C*2/*c* pyroxenes.

On the other hand, the linewidth of the mode at 670 cm^{-1} shows only a small increase between diopside and $Di_{70}En_{30}$, suggesting that disorder from the M2-M2′ substitution has a smaller effect on the tetrahedral chains, at least up to $Di_{70}En_{30}$; cation substitution typically has a small influence on the tetrahedral chain.

REFERENCES CITED

Angel, R.J., Chopelas, A., and Ross, N.L. (1992) Stability of high-density clinoenstatite at upper mantle pressures. Nature, 358, 322–324.

Benna, P., Tribaudino, M., Zanini, G., and Bruno, E. (1990) The crystal structure of $Ca_{0.8}Mg_{1.2}Si_2O_6$ clinopyroxene ($Di_{80}En_{20}$) at T = –130, 25, 400, and 700 °C. Zeitschrift für Kristallographie, 192, 183–199.

Bruno, E., Carbonin, S., and Molin, G.M. (1982) Crystal structure of Ca-rich clinopyroxenes on the $CaMgSi_2O_6$-$Mg_2Si_2O_6$ join. Tschermaks Mineralogische und Petrographische Mitteilungen, 29, 223–240.

Carpenter, M.A. (1978) Nucleation of augite at antiphase boundaries in pigeonite. Physics and Chemistry of Minerals, 2, 237–251.

Chopelas, A. and Serghiou, G. (2002) Spectroscopic evidence for pressure-induced phase transitions in diopside. Physics and Chemistry of Minerals, 29, 403–408.

Downs, R.T. (2006) The RRUFF Project: An integrated study of the chemistry, crystallography, Raman and infrared spectroscopy of minerals. Program and Abstracts of the 19th General Meeting of the International Mineralogical Association in Kobe, Japan, O03-13.

Etchepare, J. (1970) Study by Raman spectroscopy of crystalline and glassy diopside. In R.W. Douglas and B. Ellis, Eds., Amorphous Materials, p. 337–346. International Conference on Noncrystalline Solids, Wiley Interscience, London.

Huang, E., Chen, C.H., Huang, T., Lin, E.H., and Xu, J-A. (2000) Raman spectroscopic characteristics of Mg-Fe-Ca pyroxenes American Mineralogist, 85, 473–479.

Iezzi, G., Della Ventura, G., Tribaudino, M., Nemeth, P., Margiolaki, I., Cavallo, A., Gaillard, F., and Behrens, H. (2010) Phase transition induced by solid solution: The ^{B}Ca-^{B}Mg substitution in richteritic amphiboles. American Mineralogist, 95, 369–381.

Mernagh, T.P. and Hoatson, D.M. (1997) Raman spectroscopic study of pyroxene structures from the Munni Munni. Journal of Raman Spectroscopy, 28, 647–658.

Moore, K.T., Veblen, D.R., and Howe, J.M. (2001) Calcium segregation at antiphase boundaries in pigeonite. American Mineralogist, 86, 1314–1318.

Morimoto, N. and Güven, N. (1970) Refinement of the crystal structure of pigeonite. American Mineralogist, 55, 1195–1209.

Newton, R.C., Charlu, T.V., Anderson, P.A.M., and Kleppa, O.J. (1979) Themochemistry of synthetic clinopyroxenes on the join $CaMgSi_2O_6$-$Mg_2Si_2O_6$. Geochimica et Cosmochimica Acta, 43, 55–60.

Ohashi, H. and Sekita, M. (1982) Raman spectroscopic study of the Si-O-Si stretching vibration in clinopyroxenes. Journal of the Japanese Association of Mineralogists, Petrologists and Economic Geologists, 77, 455–459.

Ohashi, Y. (1984) Polysynthetically-twinned structures of enstatite and wollastonite. Physics and Chemistry of Minerals, 10, 217–229.

Ohashi, Y. and Finger, L.W. (1976) The effect of Ca substitution on the structure of clinoenstatite. Carnegie Institute Washington Year Book, 75, 743–746.

Prencipe, M., Mantovani, L., Tribaudino, M., Bersani, D., and Lottici, P.P. (2012) The Raman spectrum of diopside: A comparison between *ab initio* calculated and experimentally measured frequencies. European Journal of Mineralogy, 24, 457–464.

Ross, N.L. and Reynard, B. (1999) The effect of iron on the $P2_1/c$ to $C2/c$ transition in $(Mg,Fe)SiO_3$ clinopyroxenes. European Journal of Mineralogy, 11, 585–589.

Rossi, G., Oberti, R., Dal Negro, A., Molin, G.M., and Mellini, M. (1987) Residual electron density of the M2 site in $C2/c$ clinopyroxenes relationship with bulk chemistry and sub-solidus evolution. Physics and Chemistry of Minerals, 14, 514–520.

Stalder, R., Kronz, A., and Schmidt, B.C. (2009) Raman spectroscopy of synthetic $(Mg,Fe)SiO_3$ single crystals. An analytical tool for natural orthopyroxenes. European Journal of Mineralogy, 21, 27–32.

Swamy, V., Dubrovinsky, L.S., and Matsui, M. (1996) High-temperature Raman spectroscopy and quasi-harmonic lattice dynamic simulation of diopside. Physics and Chemistry of Minerals, 24, 440–446.

Tribaudino, M. (2000) A transmission electron microscope investigation of the $C2/c \rightarrow P2_1/c$ phase transition in clinopyroxenes along the diopside-enstatite ($CaMgSi_2O_6$-$Mg_2Si_2O_6$) join. American Mineralogist, 85, 707–715.

Tribaudino, M. and Nestola, F. (2002) Average and local structure in $P2_1/c$ clinopyroxenes along the join diopside-enstatite ($CaMgSi_2O_6$-$Mg_2Si_2O_6$). European Journal of Mineralogy, 14, 549–555.

Tribaudino, M., Benna, P., and Bruno, E. (1989) Average structure and M2 site configurations in $C2/c$ clinopyroxenes along the Di-En join. Contributions to Mineralogy and Petrology, 103, 452–456.

Tribaudino, M., Prencipe, M., Nestola, F., and Hanfland, M. (2001) A $P2_1/c$-$C2/c$ high-pressure phase transition in $Ca_{0.5}Mg_{1.5}Si_2O_6$ clinopyroxene. American Mineralogist, 86, 807–813.

Tribaudino, M., Nestola, F., Cámara, F., and Domeneghetti, M.C. (2002) The high-temperature $P2_1/c$-$C2/c$ phase transition in Fe-free pyroxene ($Ca_{0.15}Mg_{1.85}Si_2O_6$): Structural and thermodynamic behaviour. American Mineralogist, 87, 648–657.

Tribaudino, M., Nestola, F., Meneghini, C., and Bromiley, G.D. (2003) The high-temperature $P2_1/c$-$C2/c$ phase transition in Fe-free Ca-rich $P2_1/c$ clinopyroxenes. Physics and Chemistry of Minerals, 30, 527–535.

Tribaudino, M., Nestola, F., and Meneghini, C. (2005) The structure behaviour of intermediate pyroxenes along the diopside-enstatite join. Canadian Mineralogist, 43, 1411–1421.

Tribaudino, M., Mantovani, L., Bersani, D., and Lottici, P.P. (2011) Raman investigation on pigeonite in ureilite. Spectroscopy Letters, 44, 480–485, DOI: 10.1080/00387010.2011.610404.

Trueblood, K.N., Bürgi, H.-B, Burzlaff, H., Dunitz, J.D., Gramaccioli, C.M., Schulz, H.H., Shmueli, U., and Abrahams, S.C. (1996) Atomic displacement parameter nomenclature. Report of a subcommittee on atomic displacement parameter nomenclature. Acta Crystallographica, A52, 770–781.

Ulmer, P. and Stalder, R. (2001) The $Mg(Fe)SiO_3$ orthoenstatite-clinoenstatite transitions at high pressures and temperatures determined by Raman-spectroscopy on quenched samples. American Mineralogist, 86, 1267–1274.

Wang, A., Jolliff, B.L., Haskin, L.A., Kuebler, K.E., and Viskupic, K.M. (2001) Characterization and comparison of structural and compositional features of planetary quadrilateral pyroxenes by Raman spectroscopy. American Mineralogist, 86, 790–806.

Wang, A., Kuebler, K., Jolliff, B.L., and Haskin, L.A. (2004) Mineralogy of a Martian meteorite as determined by Raman spectroscopy. Journal of Raman Spectroscopy, 35, 504–514.

Yu, Y.G., Wentzcovitch, R.M., and Angel, R.J. (2010) First principles study of thermodynamics and phase transition in low-pressure ($P2_1/c$) and high-pressure ($C2/c$) clinoenstatite $MgSiO_3$. Journal of Geophysical Research, 115, B02201–B02210.

MANUSCRIPT RECEIVED NOVEMBER 22, 2011
MANUSCRIPT ACCEPTED MAY 8, 2012
MANUSCRIPT HANDLED BY ROLAND STALDER